






RESEARCH ARTICLE | OCTOBER 10 2024

Machine learning force field for thermal oxidation of silicon

Lukas Cvitkovich ; Franz Fehring; Christoph Wilhelmer ; Diego Milardovich ; Dominic Waldhör ; Tibor Grasser 



J. Chem. Phys. 161, 144706 (2024)

<https://doi.org/10.1063/5.0220091>



Articles You May Be Interested In

Improving molecular force fields across configurational space by combining supervised and unsupervised machine learning

J. Chem. Phys. (March 2021)

Neural network potential from bispectrum components: A case study on crystalline silicon

J. Chem. Phys. (August 2020)

On-the-fly machine learned force fields for the study of warm dense matter: Application to diffusion and viscosity of CH

Phys. Plasmas (April 2024)



The Journal of Chemical Physics

Special Topics Open for Submissions

[Learn More](#)

Machine learning force field for thermal oxidation of silicon

Cite as: J. Chem. Phys. 161, 144706 (2024); doi: 10.1063/5.0220091

Submitted: 22 May 2024 • Accepted: 24 September 2024 •

Published Online: 10 October 2024



Lukas Cvitkovich,^{a)} Franz Fehrer, Christoph Wilhelmer, Diego Milardovich, Dominic Waldhör, and Tibor Grasser

AFFILIATIONS

Institute for Microelectronics, Technische Universität Wien, 1040 Wien, Austria

^{a)} Author to whom correspondence should be addressed: cvitkovich@iue.tuwien.ac.at

ABSTRACT

Looking back at seven decades of highly extensive application in the semiconductor industry, silicon and its native oxide SiO₂ are still at the heart of several technological developments. Recently, the fabrication of ultra-thin oxide layers has become essential for keeping up with trends in the down-scaling of nanoelectronic devices and for the realization of novel device technologies. With this comes a need for better understanding of the atomic configuration at the Si/SiO₂ interface. Classical force fields offer flexible application and relatively low computational costs, however, suffer from limited accuracy. *Ab initio* methods give much better results but are extremely costly. Machine learning force fields (MLFF) offer the possibility to combine the benefits of both worlds. We train a MLFF for the simulation of the dry thermal oxidation process of a Si substrate. The training data are generated by density functional theory calculations. The obtained structures are in line with *ab initio* simulations and with experimental observations. Compared to a classical force field, the most recent reactive force field, the resulting configurations are vastly improved. Our potential is publicly available in an open-access repository.

© 2024 Author(s). All article content, except where otherwise noted, is licensed under a Creative Commons Attribution-NonCommercial 4.0 International (CC BY-NC) license (<https://creativecommons.org/licenses/by-nc/4.0/>). <https://doi.org/10.1063/5.0220091>

I. INTRODUCTION

Silicon has played a major role in semiconductor device technology for more than half a century and continues to find a broad range of novel applications spanning from single-electron devices¹ to spintronics^{2,3} and semiconductor spin qubits.⁴

One of the most important reasons for the extensive use of Si is that its native oxide SiO₂ allows the production of semiconductor/insulator interfaces of exceptional quality.⁵ Highly optimized devices such as MOSFETs benefit from low defect densities at the interface and convenient growth of the oxide directly onto a Si substrate by thermal oxidation.⁶ Although pure SiO₂ is being gradually substituted as a gate dielectric by other materials possessing significantly higher dielectric constants,^{7,8} commonly termed as high-*k* dielectrics, the inclusion of an ultra-thin SiO₂ passivation layer on the Si substrate prior to the application of the high-*k* film remains crucial. In this regard, the SiO₂ passivation layer greatly enhances device performance, making it an essential component also in modern devices.^{9–11} Contemporary trends in the fabrication and down-scaling of device dimensions have redirected research focus toward chemical-based bottom-up fabrication methods.^{12–14} Among these

methods, the creation of ultra-thin SiO₂ layers holds paramount significance. Furthermore, as a testbed for innovative device technologies, the material system Si/SiO₂ offers an appropriate environment for long-lived spins that can be controlled coherently.^{15,16}

Ultra-thin layers of SiO₂ (on the order of a few nm) are typically fabricated through thermal oxidation of silicon. The underlying mechanisms of this process have been examined extensively over decades, through both experimental and theoretical means.^{17–23} Earlier modeling approaches, such as the seminal Deal–Grove model,¹⁷ yield good results in a progressed stage of oxidation (>15 nm oxide thickness), however, fail to describe the initial oxidation regime,^{24,25} which is important for state-of-the-art technologies that require layered materials with thicknesses on the order of a few nm. Consequently, the intricacies of the initial oxidation phase require more sophisticated models. In a previous study, based on the results of the dynamic *ab initio* molecular dynamics (AIMD) calculations, we proposed a multi-stage oxidation scheme that combined all previous experimental and theoretical insights into a comprehensive model.²⁶

In the present work, we extend our first-principles based modeling approach by a machine learning force field (MLFF). From the

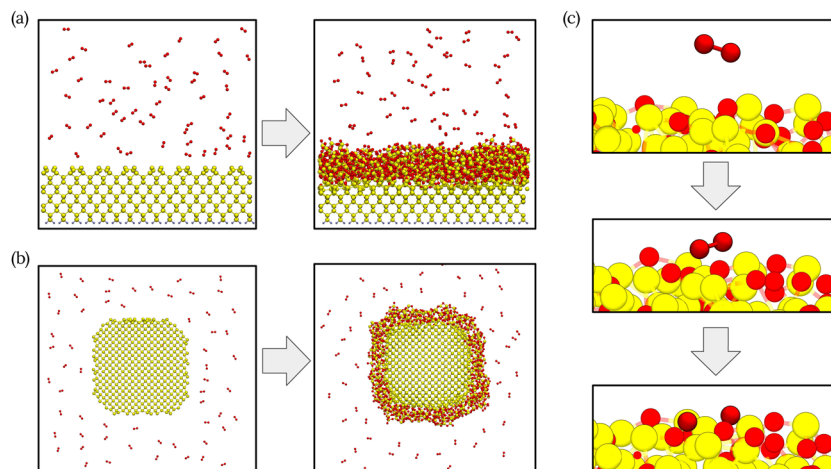


FIG. 1. Simulation procedure. (a) Reconfigured Si(100) surfaces or (b) Si nanowires are exposed to gaseous oxygen within molecular dynamics calculations. (c) The O_2 molecules spontaneously react with the surface and dissociate to form an oxide coating around the surface. After every 10 000 steps ($\Delta t = 1$ fs), the structure is optimized to avoid heating (each dissociation event releases energy), and O_2 molecules in the gas phase are refilled to maintain the pressure according to an ideal gas law.

methodological perspective, the process of thermal oxidation offers an interesting use case for machine learned interatomic potentials, as our MLFF is universally suitable for gaseous oxygen, crystalline Si, and amorphous SiO_2 . Machine learning (ML) techniques enable overcoming the strong limitations on cell sizes and simulation times, the typical drawbacks of *ab initio* calculations, while keeping the accuracy of the results practically unchanged.^{27,28} The ability to enlarge the system size and for simulating on larger time scales allows for the investigation of the growth kinetics of the oxidation process and for the generation of even more realistic models of Si/ SiO_2 interfaces, including long-range disorder and interface roughness. Furthermore, we extend our investigations from flat Si surfaces to more complex surface structures, such as cylindrical Si nanowires. As shown in Fig. 1, our ML approach allows modeling of the thermal oxidation process within dynamic simulations starting from entirely oxygen-free silicon surface structures. Within the MD simulation, these structures are exposed to an O_2 gas, which reacts with the surface and forms a coating layer of amorphous SiO_2 .

II. METHODOLOGY

Training of an MLFF typically requires the combined use of descriptors,²⁹ machine learning algorithms,³⁰ and training data. Methods and computational techniques employed in this work are described in the following.

A. Machine learning force field

Our MLFF is implemented within the Gaussian approximation potential (GAP) method.³⁰ Similar to other ML models employed in the context of interatomic potentials, GAP completely neglects the electronic structure of a given system and assumes that the potential energy can be determined solely from the atomic configuration.

The usage of unbiased metrics is essential for the training data of a ML model. For this purpose, so-called descriptors are used to generate abstract representations of the input structures. A descriptor maps the atomic structure to a mathematical object (typically a vector) and this description is invariant to rotation, translation, or the permutation of identical atoms. This approach allows reducing the size of the training dataset drastically by only providing the essential information to the ML model. Within the scope of this work, we employed the frequently used smooth overlap of atomic positions (SOAP) descriptor²⁹ in conjunction with two-body descriptors.³¹ User-defined parameters are given in Appendix A.

Our trained MLFF is available in an open-access repository, together with several oxidized interface structures and the training dataset.³²

B. DFT training data

Our MLFF is trained on data from more than 1400 density functional theory (DFT) calculations. Underlying structures include single atoms, dimers, bulk structures of Si and SiO_2 , and oxidized Si surfaces and nanowires with various oxygen coverages. Data for the initial training set are obtained by using the stepwise oxidation process, as presented in Ref. 26. In this approach, the starting points are oxygen-free Si surface structures, which become gradually oxidized within AIMD calculations. Oxygen is provided by placing O_2 molecules in the vicinity of the Si surface. This simulation procedure yields amorphous interfaces that are much more realistic than crystalline structures used in earlier computational studies.^{33–36} A comprehensive overview of the structures contained in the training dataset together with a detailed description of their generation can be found in Appendix B.

All density functional theory calculations are carried out using the CP2K package,³⁷ a code that uses the mixed Gaussian and plane waves approach (GPW). We use a double- ζ Gaussian basis set for all atom types and the well-established Goedecker–Teter–Hutter

(GTH) pseudopotentials to represent closed-shell electrons.^{38,39} The electron density is expanded using a plane-wave basis with a cut-off of 650 Ry. The exchange–correlation energy is obtained by means of the semilocal generalized gradient approximation (GGA) functional PBE. Atomic relaxations were carried out with a force convergence criterion of 15 meV/Å. Within the AIMD simulations, the total energy was conserved (microcanonical or NVE ensemble) and the total spin was restricted to 0. The two spin channels were allowed to have different spatial orbitals (unrestricted Kohn–Sham calculations).

III. RESULTS

In the following, we give an overview of the capabilities of our MLFF. To this end, we employ the MLFF to run molecular dynamics simulations of the oxidation of the Si surface. In contrast to the AIMD calculations,²⁷ where single O₂ molecules were placed above the Si surface, we now expose the Si surface to an oxygen atmosphere containing many oxygen molecules (see Fig. 1). Similar to the AIMD runs, the number of particles, the total energy, and the simulation volume are conserved (microcanonical or NVE ensemble).

A. Comparison with DFT

Validation of the ML model is done on a set of structures that are similar to the training dataset, i.e., structures of oxidized surfaces and nanowires. We compare the energies and forces predicted by DFT to the values from the ML model, as shown in Fig. 2. The deviations are estimated by the mean absolute error (MAE) between both methods. The MAE in energy is below 10 meV/atom, and the forces are predicted with an accuracy of 0.16 eV/Å. The clear linear correlation for systems with 200–5000 atoms indicates a very good agreement between DFT and the MLFF and allows ruling out systematic errors between the two.

Furthermore, our MLFF correctly reproduces the spontaneous O₂ dissociations at the Si surface²⁷ with an energy gain of around 7 eV per dissociation.

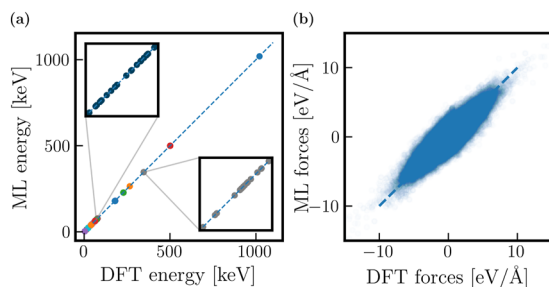


FIG. 2. Comparison between DFT and the ML model for 400 Si/oxide structures. (a) The values of the energies show excellent correlation over the full range of structures, as indicated by the dashed blue lines with slope 1. The blue and gray points shown in the insets correspond to oxidized Si(100) surfaces and oxidized nanowires, respectively. The MAE is below 10 meV/atom. (b) Good agreement between the two methods is also obtained for the inter-atomic forces with a MAE below 0.16 eV/Å.

B. Structural properties

The ML model can be further validated by the structural qualities of the resulting structures, as shown in Fig. 3. The presented results refer to a flat, oxidized Si surface,⁴⁰ which measures $6 \times 6 \text{ nm}^2$ in plane and exhibits an oxide thickness of around 1 nm. While the mean Si–O bond length of 1.63 Å is in line with the experimental values of bulk SiO₂,^{41,42} there are a number of strained bonds with a length of more than 1.8 Å. These bonds are exclusively found at the interface indicating a considerable strain in this region.

An important result is the formation of SiO₄ tetrahedrons, the building blocks of SiO₂, indicating that even ultra-thin oxide layers already exhibit the structural properties of bulk SiO₂.²⁶ The mean O–Si–O bond angle [Fig. 3(b)] matches the ideal tetrahedral bond angle of 109.47°, which means that the tetrahedrons are rigid and already form in an early stage of oxidation. The tendency to find enlarged O–Si–O bond angles (the angles between two tetrahedrons) at the interface (up to 140°) agrees with the previous observations of such interface structures.^{26,43} Further evidence for the formation of SiO₂ is provided by a coordination number analysis, as shown in Figs. 3(c) and 3(d). Most of the Si atoms in the oxide are fourfold coordinated by oxygen. Lower O-coordination can only be found at Si atoms close to the Si/oxide interface. The interface is not sharp, but represented by a transition region of 0.5 nm thickness. Within this region, the amount of oxygen increases steadily such that the O-coordination of the Si atoms increases from 0 to 4 in growth

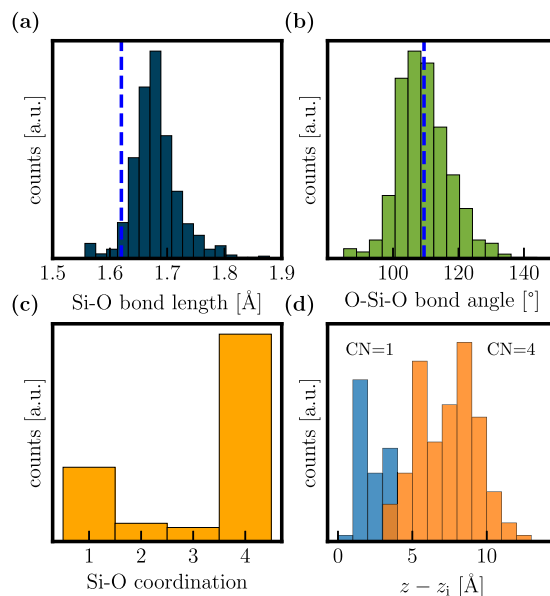


FIG. 3. Geometric measures indicating the quality of the Si/SiO₂ structures. The results are shown for a representative interface structure with an effective oxide thickness of 1 nm. (a) The Si–O bond lengths (average 1.65 Å) agree reasonably well with experimental values (dashed line) of 1.62 Å of bulk SiO₂.^{41,42} (b) Similar agreement is found for the O–Si–O bond angles, which match the optimal tetrahedral bond angle of 109.47° (dashed line). (c) The O-coordination for Si atoms ranges from 1 to 4, as expected for interfacial structures. (d) Position of Si atoms with one O neighbor (CN = 1) and four O neighbors (CN = 4). Fourfold O-coordinated Si is found in SiO₄ tetrahedrons in the oxide, while lower coordinations correspond to Si atoms close to the interface.

direction. Above the transition region, all Si atoms are fourfold O coordinated and integrated in a SiO_4 tetrahedron. Following the transition region is the crystalline Si substrate. We define the thickness of the interface/transition region d_{IF} as the distance between the first Si atom with one O neighbor to the last Si atom with less than four oxygen neighbors. These results are not only in line with the AIMD simulations from Ref. 26, they also agree with transmission electron microscope (TEM) images,^{41,44} electron-energy-loss spectroscopy (EELS),^{45,46} and photoemission studies.^{41,47}

C. Growth kinetics

As found experimentally²⁴ and confirmed theoretically by means of AIMD calculations,²⁶ the oxidation rate decreases strongly as soon as an oxide layer has formed on the initially clean Si surface. As long as the Si surface is only sparsely oxidized, that is, the surface still shows unoxidized Si dimers, O_2 molecules can spontaneously adsorb and dissociate at the surface. During this phase, the oxidation rate is limited only by the amount of oxygen interacting with the surface.

In a later stage, in which the surface is fully covered by an oxide film, the oxidation rate decreases as the limiting factor is now the diffusion of O into deeper layers of Si. The diffusion is necessary in order to make room for further dissociative surface reactions. This behavior is also captured by the MLFF. We evaluate the position of the Si/ SiO_2 interface z_i and oxide surface z_s by averaging the z -position of the five lowest and the five highest oxygen atoms, respectively. The oxide thickness t is then the difference between surface and interface $t = z_i - z_s$. Evaluating the thickness of the oxide layer by using this procedure in an MD run that simulates the thermal oxidation starting from a clean Si surface allows estimating t as a function of time, as shown in Fig. 4.⁴⁸ The oxidation rate has a maximum at the beginning and decreases significantly as soon as the surface is saturated with oxygen. At this point, O_2 molecules cannot dissociate spontaneously anymore but adsorb onto the surface where they eventually dissociate after a few ps. This behavior explains the experimentally observed decrease in oxidation rate²⁴ and is in line with previous observations from Refs. 26 and 49–51.

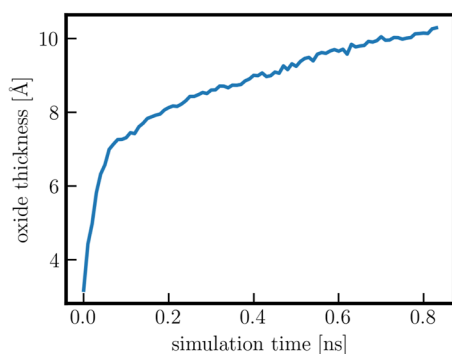


FIG. 4. Oxide thickness during dynamic oxidation of Si as a function of simulation time. Initially, fast oxidation is enabled by spontaneous surface reactions. After the surface is saturated with O, the dominant reaction mechanism changes to molecular precursor mediated dissociation, a process associated with slower oxidation rates.⁴⁹

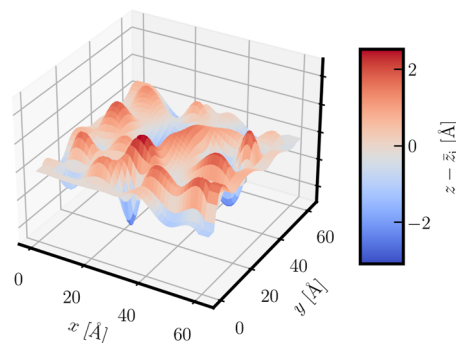


FIG. 5. Interface roughness resulting due to the dynamic oxidation process governed by random adsorption trajectories. The RMS roughness of the interface is found to be $R_q = 0.79 \text{ Å}$.

D. Interface quality

Numerous experiments have shown that the growth of SiO_2 on a Si substrate results in a significant interface and surface roughness.^{52,53} In the initial oxidation regime, the roughness increases with the oxide thickness but saturates after the oxide layer exceeds 10 nm. At this point, the oxidation rate becomes constant and the process is governed by O_2 diffusion,⁵³ as assumed within the Deal–Grove model,¹⁷ instead of O_2 surface reactions, which enable a faster oxidation in the early oxidation stages.²⁶

In order to investigate the interface roughness, we oxidize a $6 \times 6 \text{ nm}^2$ Si surface by means of the MLFF and depict the roughness of one representative Si/ SiO_2 interface resolved in the in-plane directions shown in Fig. 5. For this analysis, we take the z -position of the lowest oxygen atom in each lateral 2D bin and connect their coordinates. The interface deviates from the average interface position \bar{z}_i by up to 2.5 Å with an average deviation of $R_a = 0.57 \text{ Å}$. Typically, the interface roughness is characterized by the root mean square deviations for which we find $R_q = 0.79 \text{ Å}$ in reasonable agreement with the measured values between 0.4 and 0.9 Å reported in Ref. 53.

Furthermore, we find a mass density of around 2.5 g/cm^3 in the oxide layer, which slightly overestimates experimental values of ultra-thin $\alpha\text{-SiO}_2$ reported in the range of $2.24\text{--}2.36 \text{ g/cm}^3$.⁴¹ On the other hand, the mass density in the interface region complies with the experimental values from Ref. 41.

E. Comparison with the classical force field

In order to further validate our force-field, we compare it to one of the most commonly used classical force fields, namely, the reactive force field (reaxFF) from Ref. 54. A comparative dataset is generated by dynamically oxidizing a $3 \times 3 \text{ nm}^2$ Si surface with the same initial parameters of position and velocity from identical starting configurations. The simulation time is set to 1.4 ns integrated over 1.4×10^6 time steps. As before, after every 10^4 steps, new oxygen molecules are added to the vacuum above the surface, such that the pressure (as obtained from the ideal gas law) in the oxygen atmosphere equals 50 bar. Again, we assume a microcanonical or NVE ensemble for the dynamic simulations.

Analyzing a number of geometric properties gives the results presented in Table I. In terms of two- and three-body geometric

TABLE I. Comparison between a classical reactive force field,⁵⁴ AIMD simulations, the herein presented MLFF, and (if available) experimental values. Basic two- and three-body measures such as Si–O bond lengths and O–Si–O angles are relatively well captured by all approaches, with slightly deviating values from reaxFF. In terms of volumetric mass density, we compare the density in the interface region ρ_{IF} and in the oxide layer ρ_{OX} . Clear differences in the interface properties are indicated by the thickness of the interface d_{IF} and oxide thickness d_{OX} obtained after 1.4 ns of dynamic oxidation at 1000 K and 50 bar.

	reaxFF	AIMD ²⁶	MLFF	Expt. ^{41,44,45}
Si–O length (Å)	1.57	1.66	1.68	1.62
O–Si–O angle (°)	112.28	≈109	109.45	109.47
ρ_{IF} (g/cm ³)	2.45	2.34	2.37	2.36–2.41
ρ_{OX} (g/cm ³)	2.65	2.5	2.5	2.24–2.36
d_{IF} (nm)	1	0.5	0.5	0.5
d_{OX} (nm)	0.4	...	1	...

measures, our MLFF performs slightly better than the reaxFF potential. While the mean O–Si–O bond angles are close to the ideal tetrahedral angle, the reactive force field gives mean Si–O bond lengths of 1.55 Å (compared to the MLFF value of 1.68 Å and the experimental value of 1.62 Å^{41,42}). Furthermore, we compare the volumetric mass density in the interface region ρ_{IF} and in the oxide layer ρ_{OX} . As mentioned before, our MLFF slightly overestimates the density in the oxide layer but reproduces the density in the interfacial transition region. ReaxFF on the other hand, gives densities about 10% larger than experimental values,⁴¹ in line with implications from shortened bond lengths, in both the interface and the oxide regions of the interface structure.

The growth kinetics, however, differ substantially between the two force fields. The number of oxygen molecules that dissolved at the surface is 15% lower when using reaxFF. On the other hand, reaxFF overestimates the diffusion of oxygen, which leads to a low-density distribution of O atoms among the Si atoms in the crystal. The result is a very large interface (the transition region d_{IF} measures about 1 nm and the oxide thickness d_{OX} is only 4 Å), with lower than expected Si–O coordination, as shown in Fig. 6. To summarize, the structures obtained by reaxFF are in strong contrast to the experimental findings of Refs. 41 and 44–47, while the MLFF—similar to AIMD—reproduces much more realistic interface structures.

F. Comparison with pretrained MLFFs

Another exciting development employing ML for interatomic potentials is the rise of pretrained universal MLFFs, such as MACE-MP-0.⁵⁵ In order to compare the abilities of our MLFF to the pretrained MACE-MP-0, we conducted a simulation of the dissociation of an O₂ molecule at a Si surface. This test case already shows that the pretrained force field is not capable of modeling the oxidation process. The O₂ molecule does not move toward the Si surface and yet dissociates spontaneously 4 Å above the surface (where it was placed) without any visible interaction⁵⁶ with the Si surface. After 400 fs, one of the O atoms leaves the surface while the other one adsorbs onto the surface.

Other (simpler) test cases such as a single O₂ molecule in a box or the clean Si(100) surface can be reasonably simulated by MACE-MP-0. From this, we conclude that the pretrained ML model

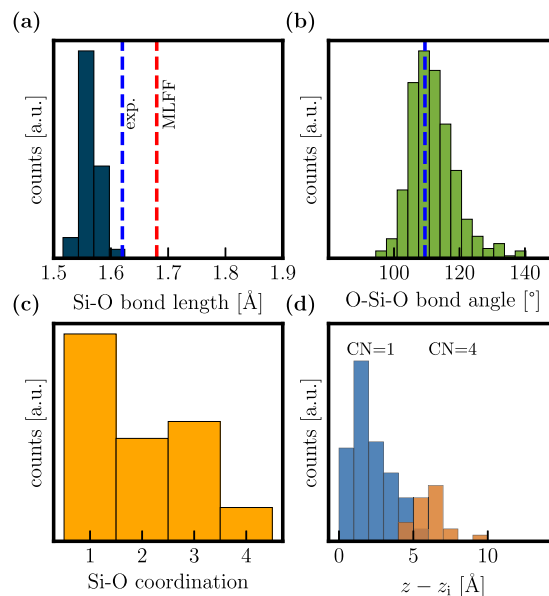


FIG. 6. Structural properties of a Si/SiO₂ interface generated by the reactive force field from Ref. 54. The plot is analogous to Fig. 3. For comparison, the experimental and averaged MLFF values for the bond lengths and the tetrahedral angles are represented by the blue and red dashed lines, respectively. With respect to the MLFF and experiments,⁴¹ reaxFF slightly underestimates bond lengths, while the tetrahedral angles are well captured. The properties of the interface, however, do not match experimental expectations, as O diffusion is overestimated by reaxFF. The number of fourfold O-coordinated Si is very low; on the other hand, there are many Si atoms with only one O neighbor. This results in a wide interface and a thin oxide layer.

has problems with treating the complex interplay between gaseous, crystalline, and amorphous materials, a use case that necessitates the training by hand.

G. Dangling bond density

Finally, the last test that we subject our model to is the determination of the dangling bond density resulting from the oxidation process. In the simplest definition, a dangling bond corresponds to a missing neighbor, that is, every Si atom with less than 4 and every O atom with less than two neighboring atoms are identified as a dangling bond.

By means of this simple analysis, we detect at least one dangling bond in 96% of the obtained interface structures. Typically, these dangling bonds do not vanish if the structure is relaxed within a subsequent DFT optimization, as this requires the breaking of other bonds, which is unlikely to happen. On average, we find 2.9 dangling bonds in structures grown on a 1.5 × 1.5 nm² Si surface area, corresponding to a dangling bond density of 1.3/nm² (130 × 10¹² cm⁻²).

Compared to the experimentally determined defect density of 0.05/nm² (5 × 10¹² cm⁻²),⁵⁷ our MLFF seems to overestimate the number of defects by almost two orders of magnitude. However, only electric spin resonance (ESR) active defects (depending on the applied bias and the location of the defect in the bandgap) appear

in the ESR measurement of Ref. 57. Another important difference between simulation and experiment is the presence of hydrogen, which is unavoidable in reality, however, completely absent in our structures. Since atomic hydrogen passivates dangling bonds⁵⁸ and, therefore, reduces the dangling bond density, a significant impact on the experimentally obtained value cannot be ruled out. Furthermore, we suspect that the density of dangling bonds in the simulated structures could be reduced by equilibrating the structure at elevated temperatures for some μ s. Given these uncertainties, we conclude that our MLFF produces structures with significantly increased dangling bond density, although a direct comparison with values inferred from ESR measurements is not valid.

A detailed analysis of the dangling bonds in the simulated structures that goes beyond the simple coordination analysis above requires thorough investigations by means of DFT. Within DFT, one can determine trap levels and relaxation energies⁵⁹ and thereby investigate whether the defects are ESR-active. We leave such extensions for the future.

IV. CONCLUSIONS

In this study, we have introduced a Gaussian approximation potential (GAP) tailored for generating ultra-thin oxide layers on a Si substrate, including amorphous interfaces between silicon and its native oxide SiO₂. The atomic structures are obtained by oxidizing an initially oxygen-free Si surface by means of molecular dynamics simulations. Starting from entirely O-free Si surfaces, the (dry) thermal oxidation process is simulated by exposing the surface to an oxygen atmosphere at 50 bar. The MLFF is capable of reproducing the intricacies of thermal oxidation in its initial stage (up to about 10 nm oxide thickness), that is, the transition from spontaneous O₂ surface reactions to molecular precursor mediated dissociations. Furthermore, the experimentally expected atomic configuration at the interface is reproduced accurately showing a 0.5 nm thick transition layer with increasing O density between the Si crystal and the oxide layer.

The credibility of our simulation framework is validated by comparison of several geometric qualities of the interface structure with experimental values, which is remarkably good in terms of bond properties and atom coordination. However, the obtained defect (or dangling bond) density significantly exceeds the experimental values, an effect that could be related to the relatively short simulation times (a few ns) compared to the experimental conditions.

Furthermore, the applicability and usefulness of our ML model is highlighted by comparison with the highly successful reactive force field (reaxFF) in its most novel version⁵⁴ as well as with the pretrained ML model MACE-MP-0.⁵⁵ In this respect, the interfaces generated by the ML model are much closer to the experimental expectations.

ACKNOWLEDGMENTS

This project has received funding from the European Research Council (ERC) under Grant Agreement No. 101055379. The computational results presented have been achieved using the Vienna Scientific Cluster (VSC). The authors acknowledge TU Wien

Bibliothek for financial support through its Open Access Funding Programme.

AUTHOR DECLARATIONS

Conflict of Interest

The authors have no conflicts to disclose.

Author Contributions

Lukas Cvitkovich: Conceptualization (lead); Data curation (equal); Formal analysis (lead); Investigation (lead); Methodology (lead); Project administration (lead); Validation (lead); Visualization (lead); Writing – original draft (lead); Writing – review & editing (lead). **Franz Fehrer:** Conceptualization (equal); Data curation (equal); Formal analysis (equal); Funding acquisition (equal); Investigation (equal); Methodology (equal); Validation (equal); Writing – review & editing (equal). **Christoph Wilhelmer:** Conceptualization (equal); Data curation (equal); Formal analysis (equal); Methodology (equal); Validation (equal); Visualization (equal); Writing – review & editing (equal). **Diego Milardovich:** Conceptualization (equal); Data curation (equal); Investigation (equal); Methodology (equal). **Dominic Waldhör:** Investigation (equal); Methodology (equal). **Tibor Grasser:** Funding acquisition (equal); Writing – review & editing (equal).

DATA AVAILABILITY

The data that support the findings of this study are available in Github at <https://github.com/lukas-cvitkovich/MLFF-SiOx>, Ref. 32.

APPENDIX A: DESCRIPTOR PARAMETERS

The descriptors can be tuned by the user via a number of parameters, as presented in Table II. The weight of each descriptor is controlled by δ , and r_{cut} is a cutoff radius, which defines a sphere within which neighboring atoms are considered. r_{Δ} is the cutoff transition width, which defines the distance needed for the descriptor cutoff to smoothly go to zero. n_{max} and l_{max} are the number of angular

TABLE II. Parameters of the employed SOAP and two-body descriptors, based on values from Ref. 28. The meaning of the parameters is given in the text (with detailed description for SOAP in Ref. 29).

Parameter	SOAP	Two-body
δ	0.4	4
r_{cut}	5	4
r_{Δ}	1	...
n_{max}	8	...
l_{max}	4	...
ζ	4	...

TABLE III. Structures in the training dataset of the GAP force field. The type of structure is given along with the number of atoms in the structure and the number of individual structures. The associated parameters σ_E and σ_F represent the regularization in the GAP corresponding to energies and forces, respectively.⁶¹

Structure type	Number of atoms	Number of structures	σ_E	σ_F
single atoms	1	3	0.0001	0.001
Si dimers	2	97	0.01	0.1
O dimers	2	57	0.01	0.1
Si–O dimers	2	23	0.01	0.1
Si–H dimers	2	52	0.01	0.1
Si bulk	192	201	0.002	0.02
SiO ₂ bulk	216	64	0.002	0.02
Clean Si surface	224	93	0.002	0.02
Ox. Si surface	232–5258	502	0.002	0.02
Si nanowire	576–1680	200	0.002	0.02
Ox. Si nanowire	1682–2063	174	0.002	0.02

and radial basis functions for the SOAP descriptor, respectively, and ζ is the power the kernel is raised to.

APPENDIX B: GENERATION OF THE TRAINING DATASET

One of the main challenges when developing an MLFF is finding suitable training data. Among the problems that can be encountered are overfitting,⁶⁰ data quality issues (incomplete or biased data), and imbalanced data (some classes of structures in the training dataset appear more frequently than others, resulting in a bias or poor performance). A detailed overview of the data used for our MLFF is presented in Table III. The dataset contains single atoms, dimers, periodic bulk structures (crystalline and amorphous), surfaces and (oxidized) nanowires (starting from Wulff-constructed 3D nanowires), and gaseous O₂. In a first step, we tried several data compositions and chose the MLFF that gave the best results (based on evaluation of the properties from Fig. 3 and Table I). This initial ML model was then used to generate new structures that were recalculated by DFT. These additional data were then implemented into the training dataset presented in Table III. With these data, we obtain the final MLFF.

Our efforts to further improve the MLFF by including more data into the training dataset gave the opposite result: the performance decreased. From this, we conclude that the model is prone to overfitting. One of the ways to avoid overfitting is the so-called “early stopping strategy.”⁶⁰ Since the MLFF already gave satisfying results in its second iteration, with decreasing performance for larger training sets, we decided to stop at this point.

REFERENCES

¹L. Guo, E. Leobandung, and S. Y. Chou, *Science* **275**, 649 (1997).

²R. Jansen, *Nat. Mater.* **11**, 400 (2012).

³I. Žutić, J. Fabian, and S. Das Sarma, *Rev. Mod. Phys.* **76**, 323 (2004).

⁴F. A. Zwanenburg, A. S. Dzurak, A. Morello, M. Y. Simmons, L. C. L. Hollenberg, G. Klimeck, S. Rogge, S. N. Coppersmith, and M. A. Eriksson, *Rev. Mod. Phys.* **85**, 961 (2013).

⁵M. Razeghi, in *Technology of Quantum Devices*, 1st ed. (Springer US, 2010), Chap. 2, pp. 41–82.

⁶S. T. Pantelides, S. Wang, A. Franceschetti, R. Buczko, M. Di Ventra, S. N. Rashkeev, L. Tsetseris, M. Evans, I. Batyrev, L. C. Feldman, S. Dhar, K. McDonald, R. A. Weller, R. Schrimpf, D. Fleetwood, X. Zhou, J. R. Williams, C. C. Tin, G. Chung, T. Isaacs-Smith, S. Wang, S. Pennycook, G. Duscher, K. Van Benthem, and L. Porter, *Silicon Carbide and Related Materials 2005, Materials Science Forum* (Trans Tech Publications Ltd., 2006), Vol. 527, pp. 935–948.

⁷M. M. Waldrop, *Nature* **530**, 144 (2016).

⁸Y. Illarionov, T. Knobloch, and T. Grasser, *Nat. Electron.* **3**, 442 (2020).

⁹R. de Almeida and I. Baumvol, *Surf. Sci. Rep.* **49**, 1 (2003).

¹⁰C. Mahata, I.-K. Oh, C. M. Yoon, C. W. Lee, J. Seo, H. Algadi, M.-H. Sheen, Y.-W. Kim, H. Kim, and T. Lee, *J. Mater. Chem. C* **3**, 10293 (2015).

¹¹A. Nakajima, Q. D. Khosru, T. Yoshimoto, and S. Yokoyama, *Microelectron. Reliab.* **42**, 1823 (2002).

¹²O. Nur and M. Willander, “Chapter 4—New emerging nanofabrication methods,” in *Low Temperature Chemical Nanofabrication, Micro and Nano Technologies*, edited by O. Nur and M. Willander (William Andrew Publishing, 2020), pp. 87–147.

¹³Q. Yao, X. Ma, H. Wang, Y. Wang, G. Wang, J. Zhang, W. Liu, X. Wang, J. Yan, Y. Li, and W. Wang, *Nanomaterials* **11**, 955 (2021).

¹⁴C. Krzeminski, G. Larrieu, J. Penaud, E. Lampin, and E. Dubois, *J. Appl. Phys.* **101**, 064908 (2007).

¹⁵M. Veldhorst, J. C. C. Hwang, C. H. Yang, A. W. Leenstra, B. de Ronde, J. P. Dehollain, J. T. Muhonen, F. E. Hudson, K. M. Itoh, A. Morello, and A. S. Dzurak, *Nat. Nanotechnol.* **9**, 981 (2014).

¹⁶L. Cvitkovich, P. Stano, C. Wilhelmer, D. Waldhör, D. Loss, Y.-M. Niquet, and T. Grasser, “Coherence limit due to hyperfine interaction with nuclei in the barrier material of Si spin qubits,” *arXiv:2405.10667* [cond-mat.mes-hall] (2024).

¹⁷B. E. Deal and A. S. Grove, *J. Appl. Phys.* **36**, 3770 (1965).

¹⁸A. Bongiorno and A. Pasquarello, *Phys. Rev. Lett.* **93**, 086102 (2004).

¹⁹A. Pasquarello, M. S. Hybertsen, and R. Car, *Nature* **396**, 58 (1998).

²⁰F. J. Himpsel, F. R. McFeely, A. Taleb-Ibrahimi, J. A. Yarmoff, and G. Hollinger, *Phys. Rev. B* **38**, 6084 (1988).

²¹T. Akiyama and H. Kageshima, *Surf. Sci.* **576**, L65 (2005).

²²E. P. Gusev, H. C. Lu, T. Gustafsson, and E. Garfunkel, *Phys. Rev. B* **52**, 1759 (1995).

²³E. Rosencher, A. Straboni, S. Rigo, and G. Amsel, *Appl. Phys. Lett.* **34**, 254 (1979).

²⁴M. A. Hopper, R. A. Clarke, and L. Young, *J. Electrochem. Soc.* **122**, 1216 (1975).

²⁵K. Ohsawa, Y. Hayashi, R. Hasunuma, and K. Yamabe, *J. Phys.: Conf. Ser.* **191**, 012031 (2009).

²⁶L. Cvitkovich, D. Waldhör, A.-M. El-Sayed, M. Jech, C. Wilhelmer, and T. Grasser, *Appl. Surf. Sci.* **610**, 155378 (2023).

²⁷O. T. Unke, S. Chmiela, H. E. Sauceda, M. Gastegger, I. Poltavsky, K. T. Schütt, A. Tkatchenko, and K.-R. Müller, *Chem. Rev.* **121**, 10142 (2021).

²⁸D. Milardovich, C. Wilhelmer, D. Waldhoer, L. Cvitkovich, G. Sivaraman, and T. Grasser, *J. Chem. Phys.* **158**, 194802 (2023).

²⁹A. P. Bartók, R. Kondor, and G. Csányi, *Phys. Rev. B* **87**, 184115 (2013).

³⁰A. P. Bartók, M. C. Payne, R. Kondor, and G. Csányi, *Phys. Rev. Lett.* **104**, 136403 (2010).

³¹V. L. Deringer and G. Csányi, *Phys. Rev. B* **95**, 094203 (2017).

³²The files are available for download in an xml format, <https://github.com/lukas-cvitkovich/MLFF-SiOx>.

³³H. Kageshima and K. Shiraishi, *Phys. Rev. Lett.* **81**, 5936 (1998).

³⁴F. Fuchs, W. G. Schmidt, and F. Bechstedt, *Phys. Rev. B* **72**, 075353 (2005).

³⁵N. Takahashi, T. Yamasaki, and C. Kaneta, *Phys. Status Solidi B* **251**, 2169 (2014).

³⁶N. Salles, N. Richard, N. Mousseau, and A. Hemeryck, *J. Chem. Phys.* **147**, 054701 (2017).

³⁷J. VandeVondele, M. Krack, F. Mohamed, M. Parrinello, T. Chassaing, and J. Hutter, *Comput. Phys. Commun.* **167**, 103 (2005).

³⁸J. VandeVondele and J. Hutter, *J. Chem. Phys.* **127**, 114105 (2007).

- ³⁹S. Goedecker, M. Teter, and J. Hutter, *Phys. Rev. B* **54**, 1703 (1996).
- ⁴⁰We assess the quality of flat surfaces because they allow for simpler analysis. Nevertheless, the results for the oxidized nanowire are similar.
- ⁴¹A. C. Diebold, D. Venables, Y. Chabal, D. Muller, M. Weldon, and E. Garfunkel, *Mater. Sci. Semicond. Process.* **2**, 103 (1999).
- ⁴²R. L. Mozzi and B. E. Warren, *J. Appl. Crystallogr.* **2**, 164 (1969).
- ⁴³K. Hirose, H. Nohira, T. Koike, K. Sakano, and T. Hattori, *Phys. Rev. B* **59**, 5617 (1999).
- ⁴⁴N. Miyata, H. Watanabe, and M. Ichikawa, *Phys. Rev. B* **58**, 13670 (1998).
- ⁴⁵D. A. Muller, T. Sorsch, S. Moccio, F. H. Baumann, K. Evans-Lutterodt, and G. Timp, *Nature* **399**, 758 (1999).
- ⁴⁶D. A. Muller and G. D. Wilk, *Appl. Phys. Lett.* **79**, 4195 (2001).
- ⁴⁷J. H. Oh, H. W. Yeom, Y. Hagimoto, K. Ono, M. Oshima, N. Hirashita, M. Nywa, A. Toriumi, and A. Kakizaki, *Phys. Rev. B* **63**, 205310 (2001).
- ⁴⁸We artificially enhance the growth rate by exposing the Si surface to a large number of O₂ molecules, corresponding to a pressure in the O₂ gas of $p = 50$ bar. This is necessary as the actual oxidation time (in the range of seconds) is still well outside the scope of feasible calculations even when using the MLFF.
- ⁴⁹Y.-C. Liao, A. M. Nienow, and J. T. Roberts, *J. Phys. Chem. B* **110**, 6190 (2006).
- ⁵⁰Y. Tsuda, A. Yoshigoe, S. Ogawa, T. Sakamoto, and Y. Takakuwa, *e-J. Surf. Sci. Nanotechnol.* **21**, 30 (2022).
- ⁵¹B. Schubert, P. Avouris, and R. Hoffmann, *J. Chem. Phys.* **98**, 7593 (1993).
- ⁵²A. H. Carim and R. Sinclair, *J. Electrochem. Soc.* **134**, 741 (1987).
- ⁵³K. Ohsawa, Y. Hayashi, R. Hasunuma, and K. Yamabe, *Jpn. J. Appl. Phys.* **48**, 05DB02 (2009).
- ⁵⁴N. Nayir, A. C. T. van Duin, and S. Erkoç, *J. Phys. Chem. A* **123**, 4303 (2019).
- ⁵⁵I. Batatia, P. Benner, Y. Chiang, A. M. Elena, D. P. Kovács, J. Riebesell, X. R. Advincula, M. Asta, W. J. Baldwin, N. Bernstein, A. Bhowmik, S. M. Blau, V. Cărare, J. P. Darby, S. De, F. D. Pia, V. L. Deringer, R. Elijošius, Z. El-Machachi, E. Fako, A. C. Ferrari, A. Genreith-Schriever, J. George, R. E. A. Goodall, C. P. Grey, S. Han, W. Handley, H. H. Heenen, K. Hermansson, C. Holm, J. Jaafar, S. Hofmann, K. S. Jakob, H. Jung, V. Kapil, A. D. Kaplan, N. Karimtare, N. Kroupa, J. Kullgren, M. C. Kuner, D. Kuryla, G. Liepuoniute, J. T. Margraf, I.-B. Magdău, A. Michaelides, J. H. Moore, A. A. Naik, S. P. Niblett, S. W. Norwood, N. O'Neill, C. Ortner, K. A. Persson, K. Reuter, A. S. Rosen, L. L. Schaaf, C. Schran, E. Sivonxay, T. K. Stenczel, V. Svahn, C. Sutton, C. van der Oord, E. Varga-Umbrich, T. Vegge, M. Vondrák, Y. Wang, W. C. Witt, F. Zills, and G. Csányi, *arXiv:2401.00096* [physics.chem-ph] (2023).
- ⁵⁶Analysis of this process at a “deeper” level is not possible given the functionality of the ML potential, e.g., the ML potential does not know about charges.
- ⁵⁷A. Stesmans and V. V. Afanas'ev, *Phys. Rev. B* **57**, 10030 (1998).
- ⁵⁸J. L. Benton, C. J. Doherty, S. D. Ferris, D. L. Flamm, L. C. Kimerling, and H. J. Leamy, *Appl. Phys. Lett.* **36**, 670 (1980).
- ⁵⁹C. Willhelmer, D. Waldhoer, M. Jech, A.-M. B. El-Sayed, L. Cvitkovich, M. Walzl, and T. Grasser, *Microelectron. Reliab.* **139**, 114801 (2022).
- ⁶⁰X. Ying, *J. Phys.: Conf. Ser.* **1168**, 022022 (2019).
- ⁶¹S. Klawohn, J. P. Darby, J. R. Kermode, G. Csányi, M. A. Caro, and A. P. Bartók, *J. Chem. Phys.* **159**, 174108 (2023).